Ab initio study of the orientation effects in multiphoton ionization and high-order harmonic generation from the ground and excited electronic states of H_2^+

Dmitry A. Telnov* and Shih-I Chu†
Department of Chemistry, University of Kansas, Lawrence, Kansas 66045, USA
(Received 24 July 2007; published 11 October 2007)

We present an *ab initio* three-dimensional (3D) calculation of multiphoton ionization (MPI) and high-order harmonic generation (HHG) of the hydrogen molecular ions subject to intense linearly polarized laser pulses. The orientation of the molecular axis with respect to the polarization of the laser field can be arbitrary. The numerical procedure involves the extension of the *generalized pseudospectral* (GPS) method for nonuniform spatial discretization of the Hamiltonian and wave functions and time propagation using the split-operator technique in the energy representation. The calculations were performed for the ground and two first excited electronic states of H_2^+ at the internuclear separation $R=2.0$ a.u. The laser pulse has a sine-squared envelope and contains 20 optical cycles with the wavelength 800 nm. The dependence of MPI and HHG on the orientation angle is analyzed. We show that orientation effects are strongly affected by the symmetry of the wave function and the corresponding distribution of the electron density. While the anisotropy of MPI and HHG is rather weak for the $1\sigma_g$ state, both processes are suppressed at the orientation angle 90° for the $1\sigma_u$ state and at the angle 0° for the $1\pi_u$ state. We discuss the multiphoton resonance and two-center interference effects in the HHG spectra which can lead both to enhancement and suppression of the harmonic generation.

DOI: 10.1103/PhysRevA.76.043412 PACS number(s): 33.80.Rv, 42.65.Ky

I. INTRODUCTION

Multiphoton ionization (MPI) and high-order harmonic generation (HHG) are fundamental atomic and molecular processes in strong laser fields that continue to attract much attention in the recent past both experimentally and theoretically [1–3]. Due to the extra internuclear degree of freedom, the response of molecules to strong fields is considerably more complicated than that of atoms. On the other hand, once the relationship between molecular structures and MPI and HHG is understood, it can lead to the control of molecules to shape harmonics, sculpt attosecond pulses, and enhance the harmonic generation efficiency, etc. Thus the study of strong-field molecular physics is a subject of much current interest in science and technology. For diatomic molecules, the extra degrees of freedom are the internuclear separation R and orientation of the molecular axis with respect to the polarization of the laser field; the latter is related to the alignment of molecules by laser [4]. An important role is played by the symmetry of electronic molecular orbitals since the orientation effects manifest themselves differently for electronic states with different symmetries. In this paper, we focus our study on the accurate treatment of the orientation effects in MPI and HHG of diatomic molecules.

The simplest diatomic molecule to study orientation effects in MPI and HHG is the hydrogen molecular ion H_2^+. This system has been treated many times previously to study various multiphoton processes in strong laser fields. The main approaches adopted for three-dimensional (3D) calculations are the time-independent non-Hermitian Floquet formalisms [5] and direct numerical solution of time-dependent Schrödinger equation (TDSE) [6]. More recently, we have introduced a time-dependent generalized non-Hermitian Floquet approach for the precision calculation of MPI and HHG rates of H_2^+ as a function of the internuclear separation R for the molecules aligned in the laser field direction [7]. We found that both the MPI and HHG rates are strongly dependent on R. Further, the enhancement of higher harmonics takes place mainly at large R. Detailed study of the correlation between the behavior of MPI and HHG phenomena was also presented.

The emphasis of the present work is to explore the orientation effects in MPI and HHG not just for the ground state but also for the excited electronic states of H_2^+. Our method is based on the generalized pseudospectral (GPS) discretization of the wave functions and operators [8,9], which allows high precision electronic structure results with the use of only a modest number of grid points. For the present study, we have developed a time-dependent (TD) GPS scheme for accurate and efficient treatment of the TDSE of two-center diatomic molecular systems. The time propagation is performed using the split-operator technique with the propagator matrices constructed in the energy representation [9,10].

As the initial states of H_2^+ for solving the TDSE, we select the ground ($1\sigma_g$) and first excited ($1\sigma_u$ and $1\pi_u$) states at the internuclear separation $R=2$ a.u. Since there is no stable H_2^+ molecule in excited electronic states at this internuclear separation, these configurations may be considered as a result of a resonant excitation from the ground state by a laser field with the appropriate wavelength. Recent experiments [11] show that this way of populating the excited electronic states is quite practical. In this work, we study the fast electronic motion while the nuclei are kept at their original positions. However, possible experimental observation is not the only purpose of presenting the results for excited electronic states in the present work. As to be shown, these states

*Permanent address: Department of Physics, St. Petersburg State University, 198504 St. Petersburg, Russia. telnov@pcqnt1.phys.spbu.ru
†sichu@ku.edu

possess a symmetry quite different from that of the ground state, and the symmetry of the electronic state and the corresponding electron density distribution dramatically influence the MPI and HHG dynamics of the molecule. The electron orbitals with the same symmetry exist in stable multielectron diatomic molecules which are a subject of extensive experimental [12] and theoretical explorations recently. Multielectron systems, however, are much more difficult to treat theoretically. Approximate models such as molecular Ammosov-Delone-Krainov (ADK) [13] and Keldysh-Faisal-Reiss (KFR) [14], etc., are often used. The models, however, have their intrinsic limitations that may prevent a correct quantitative description of the phenomena. On the other hand, H_2^+ is a unique one-electron molecular system which allows for almost exact solution in the field-free case as well as for accurate treatment in the laser field. Thus the results obtained in this work for both the ground and excited electronic states of H_2^+ can provide useful insight for the understanding of MPI and HHG in multielectron diatomic and polyatomic molecules. We note that *ab initio* nonperturbative study of the MPI and HHG processes from the ground electronic states of diatomic molecules such as H_2 [15], N_2, O_2, F_2 [16], and CO [17] molecules can now be treated rather accurately by means of the self-interaction-free time-dependent density functional theory (TDDFT).

The organization of the paper is as follows. In Sec. II, we describe the version of the generalized pseudospectral discretization of wave functions and operators developed in the present work. It makes use of the prolate spheroidal coordinates and sets of grid points that allow accurate account of the boundary conditions and produce high precision wave functions and eigenvalues for moderate numbers of grid points. We also describe here our implementation of the split-operator technique for accurate and efficient time propagation of the discretized wave functions. Finally, in this section we discuss how we calculate the ionization probabilities and HHG spectra from the time-dependent wave functions. In Sec. III, we present our results regarding MPI and HHG of the ground and excited electronic states of H_2^+. The resonance and two-center interference effects in the HHG spectra are discussed in details as well as the influence of the orbital symmetry on the MPI and HHG processes. Section IV contains concluding remarks.

II. THEORY AND NUMERICAL TECHNIQUES

To calculate the ionization probability and HHG spectra, we solve the time-dependent Schrödinger equation for the molecule H_2^+ in the laser field. The initial wave function is an unperturbed eigenfunction of H_2^+. For our calculations, we select the ground $(1\sigma_g)$ and two excited $(1\sigma_u$ and $1\pi_u)$ electronic states. The nuclei are fixed at their positions, and the nuclear motion is not taken into account. To describe the diatomic molecular ion H_2^+, we make use of the prolate spheroidal coordinates ξ, η, and φ which are related to the Cartesian coordinates x, y, and z as follows [18]:

$$x = a\sqrt{(\xi^2-1)(1-\eta^2)}\cos\varphi,$$

$$y = a\sqrt{(\xi^2-1)(1-\eta^2)}\sin\varphi,$$

$$z = a\xi\eta \quad (1 \leqslant \xi < \infty, \ -1 \leqslant \eta \leqslant 1). \tag{1}$$

In Eq. (1) we assume that the molecular axis is directed along the z axis, and the nuclei are located on this axis at the positions $-a$ and a, so the internuclear separation $R=2a$.

A. Generalized pseudospectral method and solution of time-independent eigenvalue problem

First, we solve the unperturbed eigenvalue problem and obtain the eigenvalues and eigenfunctions:

$$[-\tfrac{1}{2}\nabla^2 + U(\xi,\eta)]\Psi(\xi,\eta,\varphi) = E\Psi(\xi,\eta,\varphi). \tag{2}$$

Here the kinetic energy operator in the prolate spheroidal coordinates reads as:

$$-\frac{1}{2}\nabla^2 = -\frac{1}{2a^2}\frac{1}{(\xi^2-\eta^2)}\left(\frac{\partial}{\partial\xi}(\xi^2-1)\frac{\partial}{\partial\xi} + \frac{\partial}{\partial\eta}(1-\eta^2)\frac{\partial}{\partial\eta} + \frac{\xi^2-\eta^2}{(\xi^2-1)(1-\eta^2)}\frac{\partial^2}{\partial\varphi^2}\right), \tag{3}$$

and the Coulomb interaction with the nuclei is as follows (the charge of each center is unity):

$$U(\xi,\eta) = -\frac{2\xi}{a(\xi^2-\eta^2)}. \tag{4}$$

For the unperturbed molecule, the projection m of the angular momentum onto the molecular axis is conserved. Thus the wave function $\Psi(\xi,\eta,\varphi)$ can be represented in a separable form,

$$\Psi(\xi,\eta,\varphi) = \psi_m(\xi,\eta)\exp(im\varphi), \tag{5}$$

and separate eigenvalue problems for different $|m|$ are obtained,

$$-\frac{1}{2a^2}\frac{1}{(\xi^2-\eta^2)}\left[\frac{\partial}{\partial\xi}(\xi^2-1)\frac{\partial}{\partial\xi} + \frac{\partial}{\partial\eta}(1-\eta^2)\frac{\partial}{\partial\eta} - \frac{m^2}{\xi^2-1} - \frac{m^2}{1-\eta^2}\right]\psi_m - \frac{2\xi}{a(\xi^2-\eta^2)}\psi_m = E\psi_m. \tag{6}$$

To solve Eq. (6), we first convert it to equivalent variational forms, different for even and odd m. This is done to ensure accurate numerical solutions of the differential equations for both even and odd projections of angular momentum [note that the *exact* eigenfunctions have factors $(\xi^2-1)^{|m|/2}(1-\eta^2)^{|m|/2}$ which are nonanalytical at nuclei for odd $|m|$]. The variational forms of Eq. (6) and detailed description of GPS discretization of the coordinates ξ and η can be found in the Appendix.

The matrix eigenvalue problems which appear upon discretization of Eq. (6) can be written as follows for even m values,

$$\sum_{i'j'}\left[T^e_{ij;i'j'} + \left(\frac{m^2}{2a^2(\xi_i^2-1)(1-\eta_j^2)} - \frac{2\xi_i}{a(\xi_i^2-\eta_j^2)}\right)\delta_{ii'}\delta_{jj'}\right]\phi_{m;i'j'} = E\phi_{m;ij}, \tag{7}$$

and odd m values,

$$\sum_{i'j'}\left[T^{o}_{ij;i'j'}+\left(\frac{m^2-1}{2a^2(\xi_i^2-1)(1-\eta_j^2)}+\frac{1+\xi_i^{-2}}{a^2(\xi_i^2-\eta_j^2)}-\frac{2\xi_i}{a(\xi_i^2-\eta_j^2)}\right)\delta_{ii'}\delta_{jj'}\right]\phi_{m;i'j'}=E\phi_{m;ij}, \tag{8}$$

respectively. Here the quantities $\phi_{m;ij}$ are related to the wave function at the discretized coordinates,

$$\psi_m(\xi_i,\eta_j)=\frac{\phi_{m;ij}}{\sqrt{\xi_i'\eta_j'}}\sqrt{\frac{1-y_j^2}{1+x_i}}\frac{P_{N_x}(x_i)P'_{N_y}(y_j)}{\sqrt{\xi_i^2-\eta_j^2}}, \tag{9}$$

$P_{N_x}(x)$ and $P'_{N_y}(y)$ being the Legendre polynomial and its derivative, respectively. The kinetic energy matrices $T^{e}_{ij;i'j'}$ and $T^{o}_{ij;i'j'}$ are calculated as follows:

$$T^{e}_{ij,i'j'}=\frac{1}{2a^2}\frac{1}{\sqrt{\xi_i'\eta_j'(\xi_i^2-\eta_j^2)}}\frac{1}{\sqrt{\xi_{i'}'\eta_{j'}'(\xi_{i'}^2-\eta_{j'}^2)}}\times\left(\delta_{jj'}\sqrt{1+x_i}\sqrt{1+x_{i'}}\sum_{k=1}^{N_x}\frac{\xi_k^2-1}{\xi_k'(1+x_k)}d^x_{ki}d^x_{ki'}+\delta_{ii'}\sqrt{1-y_j^2}\sqrt{1-y_{j'}^2}\sum_{k=1}^{N_y}\frac{1-\eta_k^2}{\eta_k'(1-y_k^2)}d^y_{kj}d^y_{kj'}\right) \tag{10}$$

and

$$T^{o}_{ij,i'j'}=\frac{1}{2a^2}\frac{1}{\sqrt{\xi_i'\eta_j'(\xi_i^2-\eta_j^2)}}\frac{1}{\sqrt{\xi_{i'}'\eta_{j'}'(\xi_{i'}^2-\eta_{j'}^2)}}\times\left(\delta_{jj'}\sqrt{\frac{1+x_i}{\xi_i^2-1}}\sqrt{\frac{1+x_{i'}}{\xi_{i'}^2-1}}\xi_i\xi_{i'}\sum_{k=1}^{N_x}\frac{(\xi_k^2-1)^2}{\xi_k^2\xi_k'(1+x_k)}\times d^x_{ki}d^x_{ki'}+\delta_{ii'}\sqrt{\frac{1-y_j^2}{1-\eta_j^2}}\sqrt{\frac{1-y_{j'}^2}{1-\eta_{j'}^2}}\times\sum_{k=1}^{N_y}\frac{(1-\eta_k^2)^2}{\eta_k'(1-y_k^2)}d^y_{kj}d^y_{kj'}\right). \tag{11}$$

The discretized coordinates ξ_i and η_j, as well as the collocation points x_i and y_j, are defined in the Appendix. Note that the potential terms are diagonal in the pseudospectral method. They are represented by their values at the discretized coordinates, so no calculation of potential energy matrix elements is required. The kinetic energy matrices are given by simple analytical expressions (10) and (11) which can be readily programmed into the computer code. Straightforward programming implementation and high accuracy for moderate number of collocation points constitute the most attractive features of the generalized pseudospectral method.

Solving the eigenvalue problems (7) and (8), we obtain unperturbed energy values and eigenstates of H_2^+, which are used as initial states for time propagation as well as for construction of propagation matrices.

B. Solution of the time-dependent Schrödinger equation in the laser field

The time-dependent Schrödinger equation in the laser field is solved by means of the split-operator method in the energy representation previously developed for our Floquet calculations [7,19]. We employ the following split-operator, second-order short-time propagation formula:

$$\Psi(t+\Delta t)=\exp(-i\tfrac{1}{2}\Delta t H_0)\exp[-i\Delta t V(\xi,\eta,t+\tfrac{1}{2}\Delta t)]\times\exp(-i\tfrac{1}{2}\Delta t H_0)\Psi(t)+O((\Delta t)^3). \tag{12}$$

Here Δt is the time propagation step, H_0 is the unperturbed electronic Hamiltonian which includes the kinetic energy and the interaction with the nuclei, $V(\xi,\eta,t)$ is the term due to the coupling to the external field. We assume that the laser field is linearly polarized and the dipole approximation is well justified. Without loss of generality, we can also assume that the polarization vector of the field lies in the plane x-z. Then using the length gauge, we can write the potential $V(\xi,\eta,t)$ in the following form:

$$V(\xi,\eta,\varphi,t)=aF(t)(\xi\eta\cos\beta+\sqrt{(\xi^2-1)(1-\eta^2)}\cos\varphi\sin\beta). \tag{13}$$

Here β is the angle between the polarization vector of the laser field and the molecular axis. The time-dependent function $F(t)$ contains the carrier and envelope factors. In our calculations, we use the sine-squared pulse shape, then the function $F(t)$ can be written as follows:

$$F(t)=F_0\sin^2\frac{\pi t}{T}\sin\omega_0 t. \tag{14}$$

In Eq. (14), F_0 is the peak field amplitude, ω_0 is the carrier frequency, and T is a pulse duration. Our pulse contains 20 optical cycles.

The time propagation process based on Eq. (12) can be described as follows. Since the unperturbed Hamiltonian commutes with the projection of the angular momentum on the molecular axis, the field-free propagator $\exp(-i\frac{1}{2}\Delta t H_0)$ is block diagonal and can be represented in the following form:

$$\exp(-i\tfrac{1}{2}\Delta t H_0)=\sum_{m=-\infty}^{\infty}\exp(-i\tfrac{1}{2}\Delta t H_0^{(|m|)})|m\rangle\langle m|, \tag{15}$$

where $H_0^{(|m|)}$ are the unperturbed Hamiltonians corresponding to particular angular momentum projections m, as expressed by Eqs. (7) and (8), and $|m\rangle\langle m|$ are the projecting operators onto the states with definite m. The propagator matrices $\exp(-i\frac{1}{2}\Delta t H_0^{(|m|)})$ are built of the unperturbed eigenvectors $\psi_k^{(|m|)}$ and eigenvalues $E_k^{(|m|)}$ when the eigenvalue problems (7) and (8) are solved,

$$\exp(-i\tfrac{1}{2}\Delta t H_0^{(|m|)})=\sum_k\exp(-i\tfrac{1}{2}\Delta t E_k^{(|m|)})|\psi_k^{(|m|)}\rangle\langle\psi_k^{(|m|)}|. \tag{16}$$

Working in the energy representation, we can control the contributions to the sum (16). For example, removing the contributions with very high energies, we can get rid of spu-

rious transitions to irrelevant regions of the energy spectrum and improve the numerical stability of the propagation. To apply the propagator in the form (15), we expand the total time-dependent wave function in the Fourier series with respect to the angular coordinate φ,

$$\Psi(\xi,\eta,\varphi,t)=\sum_{m=-\infty}^{\infty}\psi_m(\xi,\eta,t)\exp(im\varphi). \tag{17}$$

Then each term in the series (17) is acted upon by only one term in the series (15), and the result of the field-free propagation can be written as follows:

$$\Psi^{(1)}(\xi,\eta,\varphi,t)\equiv\exp(-i\tfrac{1}{2}\Delta tH_0)\Psi(\xi,\eta,\varphi,t)$$
$$=\sum_{m=-\infty}^{\infty}\exp(im\varphi)\exp(-i\tfrac{1}{2}\Delta tH_0^{|m|})\psi_m(\xi,\eta,t). \tag{18}$$

Using this procedure for the field-free propagation step, we can significantly reduce the dimensions of the propagator matrices and speed up the computations. In practical calculations, the infinite series (17) should be truncated. We found that for our present calculations retaining the m values -8 to 8 is sufficient to obtain converged results.

The external field operator $\exp(-i\Delta tV)$ is a multiplication in coordinate representation when using the length gauge, and the next part of the short-time propagation is achieved straightforwardly,

$$\Psi^{(2)}(\xi,\eta,\varphi,t)\equiv\exp[-i\Delta tV(\xi,\eta,\varphi,t+\tfrac{1}{2}\Delta t)]$$
$$\times\Psi^{(1)}(\xi,\eta,\varphi,t). \tag{19}$$

Then $\Psi^{(2)}(\xi,\eta,\varphi,t)$ is reexpanded in the Fourier series,

$$\Psi^{(2)}(\xi,\eta,\varphi,t)=\sum_{m=-\infty}^{\infty}\psi_m^{(2)}(\xi,\eta,t)\exp(im\varphi), \tag{20}$$

and the next unperturbed propagation is applied,

$$\Psi^{(3)}(\xi,\eta,\varphi,t)\equiv\exp(-i\tfrac{1}{2}\Delta tH_0)\Psi^{(2)}(\xi,\eta,\varphi,t)$$
$$=\sum_{m=-\infty}^{\infty}\exp(im\varphi)\exp(-i\tfrac{1}{2}\Delta tH_0^{|m|})\psi_m^{(2)}(\xi,\eta,t). \tag{21}$$

This completes the short-time propagation according to Eq. (12) since $\Psi^{(3)}$ is the wave function Ψ at the time $t+\Delta t$,

$$\Psi(\xi,\eta,\varphi,t+\Delta t)=\Psi^{(3)}(\xi,\eta,\varphi,t). \tag{22}$$

The procedure described above is to be applied sequentially starting at $t=0$ and ending at $t=T$. As a result, the wave function $\Psi(\xi,\eta,\varphi,t)$ is obtained on a uniform time grid within the interval $[0,T]$.

The numerical parameters of the present calculations are as follows. We used 72 grid points in ξ and 24 grid points in η, accordingly the dimension of the propagator matrices is 1728×1728. This coordinate grid allows to reproduce the ground state and low-lying excited states energies of H_2^+ with the machine accuracy. We keep the angular momentum projections from -8 to 8. As test calculations show, this is enough for convergence even at the highest intensity 3×10^{14} W/cm^2 used in the calculations. For the time propagation, we use 4096 time steps per optical cycle (81920 steps for the whole pulse). Again, this is a safe choice for the laser field frequency and intensities used in the calculations. For efficient matrix-vector multiplications we use basic linear algebra subroutines (BLAS) found in the Intel math kernel library (MKL). Developing a parallel computer code also helps to speed up the computations.

C. Ionization probability and high-order harmonic generation spectra

Once the wave function is computed, we can proceed to calculate the ionization probability of H_2^+ in the laser field and spectra of the produced high-order harmonic radiation. The ionization probability P_i can be calculated through the survival probability P_s,

$$P_i=1-P_s. \tag{23}$$

The latter can be defined as a probability of finding the electron within sufficiently large volume v around the nuclei,

$$P_s=\int_v d^3r|\Psi|^2. \tag{24}$$

Since we use an absorber, the normalization of the wave function is not preserved during the time propagation. The outgoing electron current is not reflected back, and the right-hand side of Eq. (24) is a decreasing function of time. The volume v is selected by inequality $\xi<20$; before the laser pulse the integral (24) is equal to unity with very high accuracy, and we assume the electron density that leaves this volume during the interaction with the laser field represents unbound states. With the time-dependent wave function $\Psi(\xi,\eta,\varphi,t)$, we can calculate the time-dependent ionization probability $P_i(t)$, and $P_i(T)$ is the ionization probability after the laser field is switched off.

To calculate HHG spectra, we employ the widely used semiclassical approach, where the basic expressions come from the classical electrodynamics but the classical quantities such as dipole moment and its acceleration are replaced with the corresponding quantum expectation values. For nonmonochromatic fields (as in our case), the spectral density of the radiation energy emitted for all the time is given by the following expression [20]:

$$S(\omega)=\frac{4\omega^4}{6\pi c^3}|\mathbf{D}_\omega|^2. \tag{25}$$

Here ω is the frequency of radiation, c is the velocity of light, and D_ω is a Fourier transform of the time-dependent dipole moment,

$$\mathbf{D}_\omega=\int_{-\infty}^{\infty}dt\mathbf{D}(t)\exp(i\omega t). \tag{26}$$

The time-dependent dipole moment is evaluated as an expectation value of the electron radius vector with the time-dependent wave function $\Psi(\xi,\eta,\varphi,t)$,

TABLE I. Energies of the ground and first excited electronic states of H_2^+ at the internuclear separation $R=2$ a.u.

State	Energy (a.u.)
$1\sigma_g$	−1.10263421449494646150896[a]
	−1.1026342144949[b]
$1\sigma_u$	−0.66753439220238293036197[a]
	−0.6675343922024[b]
$1\pi_u$	−0.42877181898585643631396[a]
	−0.4287718198959[b]
$2\sigma_g$	−0.36086487533950384503869[a]
	−0.3608648753383[b]
$2\sigma_u$	−0.25541316508648456141725[a]
	−0.2554131650857[b]

[a]Present work.
[b]Reference [21].

$$\mathbf{D}(t) = \langle \Psi | \mathbf{r} | \Psi \rangle. \tag{27}$$

The total energy $\mathcal{E}$ emitted in the harmonic radiation can be calculated as

$$\mathcal{E} = \int_0^\infty d\omega S(\omega). \tag{28}$$

For a single laser pulse (14), the radiation energy spectrum (25) contains peaks corresponding to odd harmonics of the carrier frequency ω_0. The width of a peak is inverse proportional to the pulse duration.

III. RESULTS AND DISCUSSION

First, we have performed the field-free calculations of the electronic eigenstates of H_2^+ at the internuclear separation 2 a.u. We do not list all the eigenvalues as they are well-known in the literature (see, e.g., [21]). In Table I the energies of the first five bound states are compared with the previous most accurate results. Note that the number of grid points we use is intended for accurate propagation involving the continuum states and well in excess for accurate description of low-lying bound states. For example, to achieve 14 digit accuracy for the ground state energy with the present discretization scheme, it is sufficient to have only 14 and 10 grid points in the ξ and η coordinates, respectively. The eigenvalues shown in Table I are computed with 16 byte representation of real numbers, all digits are accurate. Although such accuracy exceeds the limits of applicability of Eq. (2), the results can be used as numerical reference data. Thus the GPS method with the parameters given above can reproduce the initial states for the time propagation procedure as well as the propagation matrices with sufficiently high accuracy.

We have also computed the electron densities of $1\sigma_g$, $1\sigma_u$, and $1\pi_u$ orbitals at $R=2$ a.u. The ground $1\sigma_g$ state density manifests an almost spherical symmetry, and one can expect a relatively smooth dependence of MPI probability and HHG energy spectra on the orientation angle between the molecular axis and the polarization direction of the laser field. On the contrary, the excited states have distinct features which are responsible for more anisotropic density distributions. These are the nodal plane perpendicular to the molecular axis for the $1\sigma_u$ state, and the molecular axis for the $1\pi_u$ state where the wave function exactly turns zero. As a result, one can expect a sharper angular dependence of MPI probability and HHG energy than in the case of $1\sigma_g$ state with prominent minima at 90° for $1\sigma_u$ and at 0° for $1\pi_u$.

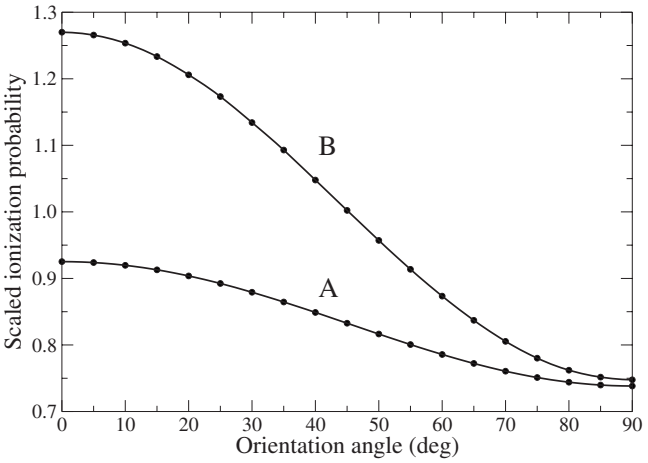

FIG. 1. Scaled MPI probabilities of the ground $1\sigma_g$ state of H_2^+ for the laser field peak intensities 1×10^{14} W/cm^2 (*A*) and 3×10^{14} W/cm^2 (*B*) vs the orientation angle β. The probabilities are obtained by multiplying the data by 10^{-5} (*A*) and 10^{-4} (*B*).

A. Multiphoton ionization

We have computed the probabilities of multiphoton ionization as functions of the orientation angle for the following peak intensities of the laser field: 1×10^{14} and 3×10^{14} W/cm^2 for the $1\sigma_g$ state, 5×10^{13} and 1×10^{14} W/cm^2 for the $1\sigma_u$ state, and 5×10^{12} W/cm^2 for the $1\pi_u$ state. In all cases we used a 20-optical cycles laser pulse with the sine-squared envelope and the carrier frequency $\omega_0=0.056\,95$ a.u. corresponding to the wavelength 800 nm. In the weak field limit, the minimum number of photons with the frequency ω_0 required for ionization is 20 for the ground state, 12 for the $1\sigma_u$ state, and 8 for the $1\pi_u$ state. With increasing the peak intensity, the minimum number of photons becomes larger mainly due to the increase of the ponderomotive potential U_p. The results are presented in Figs. 1–3. As expected, the dependence of MPI probability P_i on the orientation angle β is not strong for the $1\sigma_g$ state. The probability is decreasing monotonously with β increasing from 0° to 90°. For the intensity 3×10^{14} W/cm^2, the ratio $P_i(0°)/P_i(90°)$ is equal to 1.7 what is in a fairly good agreement with the results of Ref. [22] ($\approx$2), where a different pulse shape was used. Note that this ratio becomes larger with increasing laser peak intensity; for the intensity 1×10^{14} W/cm^2, $P_i(0°)/P_i(90°)=1.25$. The same trend can be observed in the calculations of Ref. [22]. These results mean that deformations of the electron density become very significant at the specified intensities and give rise to more anisotropic ionization for more intense fields. Such density

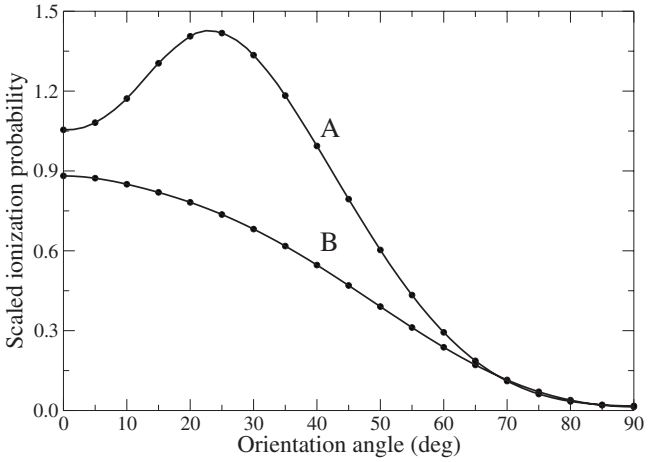

FIG. 2. Scaled MPI probabilities of the $1\sigma_u$ state of H_2^+ for the laser field peak intensities 5×10^{13} W/cm^2 (A) and 1×10^{14} W/cm^2 (B) vs the orientation angle β. The probabilities are obtained by multiplying the data by 10^{-3} (A) and 10^{-1} (B).

deformations can lead not only to quantitative but also to qualitative changes in the angular dependence of the MPI probability, as we can see for the $1\sigma_u$ state (Fig. 2).

For weaker intensity 5×10^{13} W/cm^2, the maximum in the dependence $P_i(\beta)$ is located approximately at $\beta=25°$, with the local minimum at $\beta=0°$. However, for higher intensity 1×10^{14} W/cm^2, the maximum is shifted to $\beta=0°$, and the minimum disappears. For the both intensities used in the calculations, the MPI probabilities demonstrate a deep minimum at the orientation angle 90°. This is an anticipated result based on the electron density distribution of the $1\sigma_u$ state and the fact that the interference of the contributions to the ionization amplitude from the two nuclei is always destructive for this state at $\beta=90°$. As opposed to the $1\sigma_g$ state, MPI becomes less anisotropic with increasing the laser peak intensity. The ratios of MPI probabilities at maximum and at minimum of their orientation angle dependence are summarized in Table II.

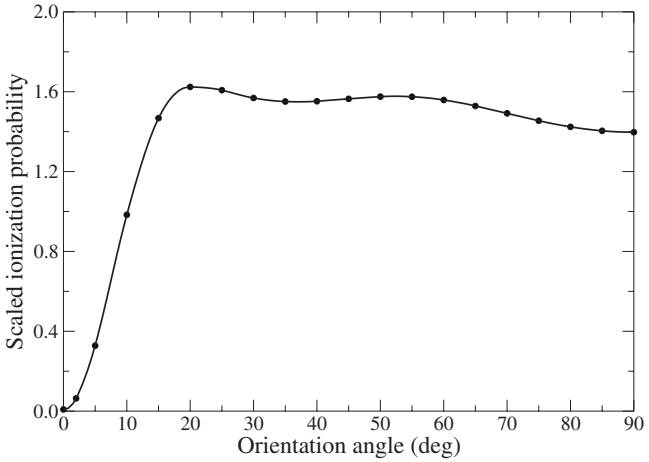

FIG. 3. Scaled MPI probability of the $1\pi_u$ state of H_2^+ for the laser field peak intensity 5×10^{12} W/cm^2. The probability is obtained by multiplying the data by 10^{-2}.

TABLE II. Ratios of MPI probabilities at maximum and at minimum of their orientation angle dependence for $1\sigma_g$ and $1\sigma_u$ electronic states of H_2^+.

State	Intensity (W/cm^2)	Max. at	Min. at	P_i^{max}/P_i^{min}
$1\sigma_g$	1×10^{14}	0°	90°	1.25
	3×10^{14}	0°	90°	1.70
$1\sigma_u$	5×10^{13}	25°	90°	81.9
	1×10^{14}	0°	90°	63.9

The calculations for the $1\pi_u$ state were performed at a low peak intensity 5×10^{12} W/cm^2. With the photon frequency ω_0, we fall in the close vicinity of a one-photon resonance with the $2\sigma_g$ state. That is why the ionization of the $1\pi_u$ state is strongly enhanced even at the low peak intensity of the laser field. An exception is made by the case $\beta=0°$, that is the laser field directed along the molecular axis. As we discussed above, the ionization of the $1\pi_u$ state should be suppressed in this case because of the specific electron density distribution. Additionally, the transition $1\pi_u\rightarrow2\sigma_g$ is not allowed at $\beta=0°$ since it requires changing the angular momentum projection that is not possible in the laser field polarized along the molecular axis. Thus the resonance enhancement of ionization does not occur at $\beta=0°$, and the MPI probability here is two orders of magnitude lower than at $\beta=20°$, where the orientation angle dependence has its maximum.

B. High-order harmonic generation

We have performed calculations of the HHG energy spectra emitted by H_2^+ in the $1\sigma_g$ and $1\sigma_u$ electronic states for various orientation angles. We used the peak intensities 3×10^{14} and 1×10^{14} W/cm^2 for the $1\sigma_g$ state and 1×10^{14} W/cm^2 for the $1\sigma_u$ state. According to the well-known atomic recollision model [23], the HHG spectra demonstrate a plateau region with a cutoff at the energy $|E_i|+3.17U_p$ where $|E_i|$ is the ionization energy of the initial state and U_p is the ponderomotive potential. For the linearly polarized laser field, $U_p=I/(4\omega_0^2)$, I being the field intensity. For diatomic molecules, besides the collision with the parent core which resembles the single atom case and leads to the same harmonic spectrum cutoff position irrespectively of the laser field intensity and internuclear separation, the collisions can occur also with the other nucleus. In the latter case, the return kinetic energy of the electron depends on the field intensity and frequency as well as on the distance between the nuclei [24]. For the field parameters used in the present calculations, two different classical trajectories may be responsible for the high kinetic energy of the electron when it returns to the other nucleus. However, the corresponding maximum recombination energies appear quite close to the atomic energy $|E_i|+3.17U_p$.

For the initial state and peak field intensities used in our calculations, the cutoff positions are supposed to be at $56\omega_0$ and $32\omega_0$ for the $1\sigma_g$ state and at $24\omega_0$ for the $1\sigma_u$ state,

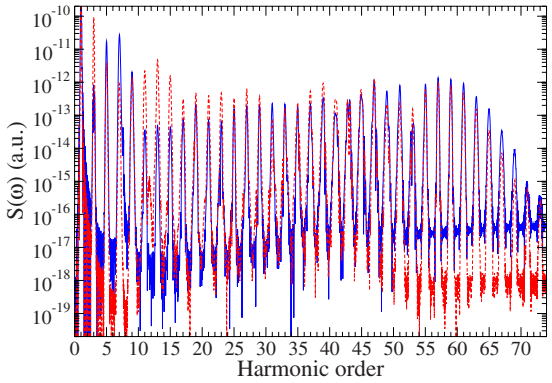

FIG. 4. (Color online) HHG spectrum $S(\omega)$ from $1\sigma_g$ state of H_2^+ for the laser field peak intensity 3×10^{14} W/cm^2 and orientation angles 0° (solid line) and 90° (dashed line).

respectively. The HHG spectrum $S(\omega)$ is shown in Figs. 4 and 5 for the $1\sigma_g$ state and in Fig. 6 for the $1\sigma_u$ state. As one can see, the semiclassically predicted cutoff positions are in fair agreement with our calculations. For the $1\sigma_g$ state, the HHG spectra at $\beta=0°$ and $\beta=90°$ are comparable in their intensity; it is also the case for all intermediate orientation angles. This observation is in full agreement with the MPI results which do not show any significant anisotropy for the $1\sigma_g$ state. One can notice the resonance structures in the HHG spectra, more clearly seen for the intensity 1×10^{14} W/cm^2 (Fig. 5) since less number of harmonics is shown in this case. There are two additional strong peaks in the HHG spectra not corresponding to an odd harmonic order. The first peak is located near the 7th harmonic; we attribute it to the resonance with the first excited $(1\sigma_u)$ state. The second resonance peak appears close to the 11th harmonic; it is attributed to the resonance with the $1\pi_u$ state. Note that in accordance with the selection rules for dipole transitions, the transition $1\sigma_g \rightarrow 1\sigma_u$ is forbidden for the orientation $\beta=90°$. On the other hand, the transition $1\sigma_g \rightarrow 1\pi_u$ is forbidden for $\beta=0°$. That is why the HHG spectra shown in Fig. 5 have only one resonance structure each. For the intermediate orientation angles, both resonance structures appear on the same HHG spectrum.

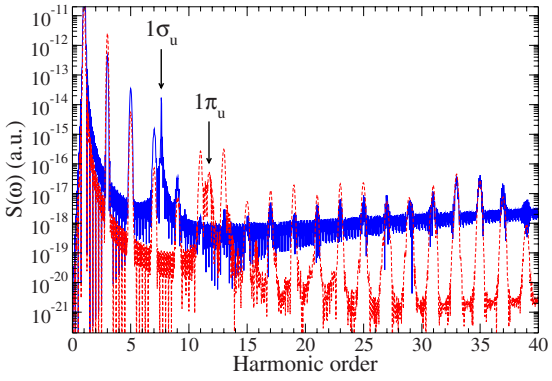

FIG. 5. (Color online) HHG spectrum $S(\omega)$ from $1\sigma_g$ state of H_2^+ for the laser field peak intensity 1×10^{14} W/cm^2 and orientation angles 0° (solid line) and 90° (dashed line). Arrows mark the resonance peaks in the spectrum.

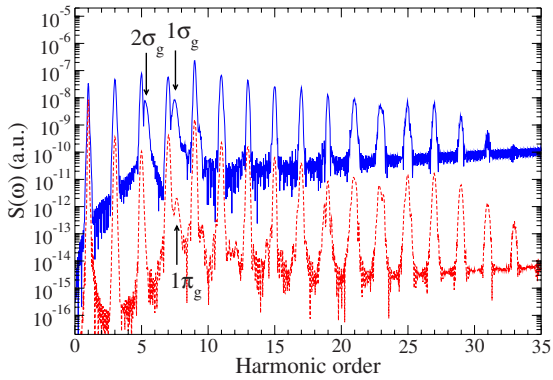

FIG. 6. (Color online) HHG spectrum $S(\omega)$ from $1\sigma_u$ state of H_2^+ for the laser field peak intensity 1×10^{14} W/cm^2 and orientation angles 15° (solid line) and 90° (dashed line). Arrows mark the resonance peaks in the spectrum.

In the vicinity of a resonance, the harmonic radiation is strongly enhanced. Thus we can see that the 7th harmonic at $\beta=0°$ is much more intense than the same harmonic at $\beta=90°$, and the 11th and 13th harmonics at $\beta=90°$ are two orders of magnitude stronger than the harmonics at $\beta=0°$. The resonance transition $1\sigma_g \rightarrow 1\sigma_u$ also affects the HHG spectra produced in the $1\sigma_u$ state. In Fig. 6 we show $S(\omega)$ for the orientation angles $\beta=15°$ and $\beta=90°$. We choose $\beta=15°$ instead of $\beta=0°$ because the resonance structures are more pronounced at this orientation angle. We attribute this result to fine tuning into the resonance while changing β due to different ac Stark energy level shifts at different orientation angles. Unlike the case of HHG radiation from the $1\sigma_g$ state, the resonance between $1\sigma_u$ and $1\sigma_g$ does not lead to enhancement of the harmonic radiation in the vicinity of the resonance energy since it essentially populates the low-lying $1\sigma_g$ state. In general, for the initial $1\sigma_u$ state the HHG signal decreases when the orientation angle is increased from 0° to 90°. As one can see from Fig. 6, the signal at $\beta=90°$ is several orders of magnitude weaker than that at $\beta=15°$. The same behavior we observed for the ionization signal (see Sec. III A above).

Recently there was an active discussion in the literature [22,25,26] regarding the interference effects in the harmonic spectra due to the two-center nature of diatomic molecules. Based on a simple recollision model, Lein *et al.* [25] suggested that the position of the interference minimum in the harmonic spectrum is given by the relation

$$R\cos\beta = \lambda/2, \tag{29}$$

where R is the internuclear separation, and λ is the de Broglie wavelength of the recolliding electron. Provided all the kinetic energy of the electron is converted into the harmonic photon energy, Eq. (29) can be recast as

$$\cos\beta = \frac{\pi}{R\sqrt{2N\omega_0}}, \tag{30}$$

with N being the harmonic order. It follows from Eq. (30) that not all harmonics can exhibit minimum in their intensity while the angle β is varied. For the parameters of our calcu-

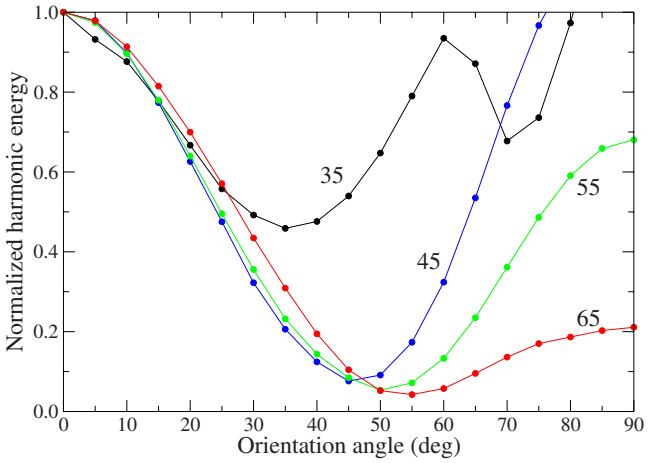

FIG. 7. (Color online) Harmonic signal from $1\sigma_g$ state of H_2^+ for the laser field peak intensity 3×10^{14} W/cm^2 as a function of orientation angle β. The harmonic signal is normalized to unity at $\beta=0$. Shown are harmonics 35, 45, 55, 65; the curves are marked with the harmonic order.

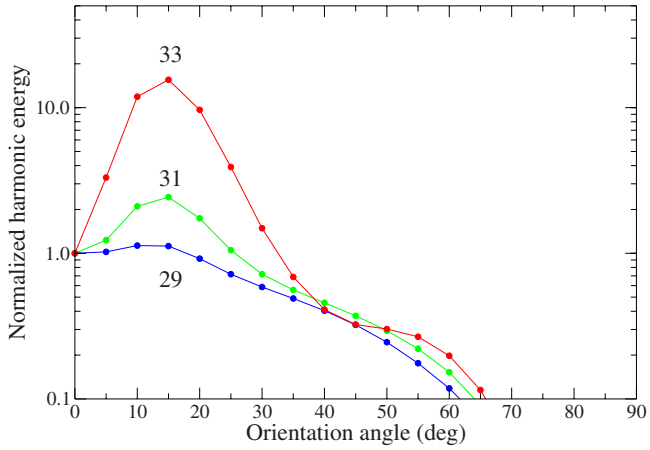

FIG. 8. (Color online) Harmonic signal from $1\sigma_u$ state of H_2^+ for the laser field peak intensity 1×10^{14} W/cm^2 as a function of orientation angle β. The harmonic signal is normalized to unity at $\beta=0$. Shown are harmonics 29, 31, 33; the curves are marked with the harmonic order.

lations ($R=2$ a.u., $\omega_0=0.056\,95$ a.u.), we find that $N\geqslant 23$. In Fig. 7 we show the angular dependence of the harmonic signal for several harmonics in the plateau region for the laser peak intensity 3×10^{14} W/cm^2. For better viewing, all the signals are normalized to unity at $\beta=0°$. As one can see, the harmonic signals for $N=35$, 45, 55, and 65 have broad minima in their dependence on the orientation angle β. The positions of the minima are in remarkable agreement with the predictions of Eq. (30). However, agreement is not that good for the laser peak intensity 1×10^{14} W/cm^2. The harmonics still exhibit minima in their orientation angle dependence but the minima positions are shifted to larger angles as compared with the predictions of Eq. (30). That means, for weaker intensities the simple semiclassical model that leads to Eq. (30) becomes less accurate. The results regarding the interference minima are summarized in Table III.

For the $1\sigma_u$ initial state, the same recollision model of HHG as in the case of the $1\sigma_g$ state can be applied. However, now Eqs. (29) and (30) point at the maxima rather than minima in the harmonic spectra. The results of our calculations are presented in Fig. 8. Again, for better viewing on the same graph, the signals of different harmonics are normalized to unity at $\beta=0°$. While for the 29th harmonic the maximum is weak, it is well shaped for the harmonics 31 and 33. Unfortunately, these harmonics are already at cutoff of the HHG spectrum and we cannot continue the analysis to higher harmonics. To extend the plateau region in the HHG spectrum, one needs to use higher peak intensities (for the same carrier frequency). However, using higher intensities will result in complete ionization of the system since even at the intensity 1×10^{14} W/cm^2 the ionization probability of the $1\sigma_u$ state is high. The positions of the interference maxima in Fig. 8 (12°–14°) are not in a good agreement with predictions of Eq. (30) (30°–36°). As in the case of the $1\sigma_g$ state, it confirms that the intensity 1×10^{14} W/cm^2 is probably too weak for the semiclassical recollision model to produce accurate results. For the $1\sigma_u$ state, however, the maxima positions obtained from our calculations are shifted to smaller angles with respect to those from Eq. (30).

TABLE III. Interference minima positions for several harmonics for the peak laser intensities 3×10^{14} W/cm^2 and 1×10^{14} W/cm^2 from the $1\sigma_g$ electronic state of H_2^+.

	Harmonic order					
	33	35	37	45	55	65
			Intensity 3×10^{14} W/cm^2			
Present work		36°		46°	51°	54°
Eq. (30)		38°		46°	51°	55°
			Intensity 1×10^{14} W/cm^2			
Present work	42°	45°	58°			
Eq. (30)	36°	38°	40°			

IV. CONCLUSION

In this paper we have presented *ab initio* 3D nonperturbative calculations of multiphoton ionization and high-order harmonic generation from the ground and excited electronic states of H_2^+. Our method is based on the generalized pseudospectral discretization of the wave functions and operators in prolate spheroidal coordinates followed by the time propagation of the wave function using the split-operator technique with the propagator matrices constructed in the energy representation. With moderate number of grid points, the method produces highly accurate unperturbed eigenvalues and eigenfunctions of H_2^+ and thus ensures the accuracy of the propagator matrices.

We have found that the dependence of MPI probabilities and HHG energy spectra on the orientation of the molecular axis with respect to the polarization of the laser field is essentially affected by the symmetry of the electronic state of

the molecule. For the orientations $\beta=0°$ and $\beta=90°$, MPI and HHG are suppressed by orders of magnitude for the $1\pi_u$ and $1\sigma_u$ states, respectively. Both MPI and HHG can be enhanced due to multiphoton resonances between the initial state and other bound states of the molecules. The resonance transitions are manifested as additional (not corresponding to odd harmonics of the carrier frequency) peaks in the HHG spectra. If the resonance transition is made to the state with higher energy, the ionization probability is increased as well as production of harmonics with frequencies in the vicinity of the transition energy. We also studied the two-center interference effects in the HHG spectra. Interference minima are found for the harmonics produced in the $1\sigma_g$ state, and interference maxima are observed for the harmonics from the $1\sigma_u$ state. Our results confirm the simple semiclassical theory of interference phenomena for higher laser intensity 3×10^{14} W/cm^2 while pronounced discrepancies are revealed for weaker intensity 1×10^{14} W/cm^2.

The results obtained in this work for H_2^+ can provide an insight into the dynamics of multielectron diatomic molecules in strong laser fields. For example, strong suppression of MPI and HHG for some orientations of a molecule (particularly, 0° and 90°) related to the symmetry properties of the molecular orbitals can indicate that commonly used restriction to the highest-occupied molecular orbital can be insufficient for correct description of orientation effects in multielectron molecules. The work on multielectron diatomic molecules by means of the self-interaction-free time-dependent density functional theory is in progress.

ACKNOWLEDGMENTS

This work was partially supported by the Chemical Sciences, Geosciences and Biosciences Division of the Office of Basic Energy Sciences, Office of Sciences, Department of Energy, by the National Science Foundation.

APPENDIX: DETAILED EXPRESSIONS FOR GENERALIZED PSEUDOSPECTRAL DISCRETIZATION IN PROLATE SPHEROIDAL COORDINATES

The variational forms of Eq. (6) are as follows:

$$\delta\left\{\frac{1}{2a^2}\int_1^\infty d\xi\int_{-1}^1 d\eta\left[(\xi^2-1)\frac{\partial\psi_m^*}{\partial\xi}\frac{\partial\psi_m}{\partial\xi}+(1-\eta^2)\frac{\partial\psi_m^*}{\partial\eta}\frac{\partial\psi_m}{\partial\eta}+\left(\frac{m^2}{\xi^2-1}+\frac{m^2}{1-\eta^2}\right)\psi_m^*\psi_m\right]-\frac{2}{a}\int_1^\infty d\xi\int_{-1}^1 d\eta\xi\psi_m^*\psi_m-E\int_1^\infty d\xi\int_{-1}^1 d\eta(\xi^2-\eta^2)\psi_m^*\psi_m\right\}=0 \tag{A1}$$

for even $|m|$ and

$$\delta\left\{-\frac{2}{a}\int_1^\infty d\xi\int_{-1}^1 d\eta\xi\psi_m^*\psi_m+\frac{1}{2a^2}\int_1^\infty d\xi\int_{-1}^1 d\eta\times\left[\frac{(\xi^2-1)^2}{\xi^2}\frac{\partial}{\partial\xi}\left(\frac{\xi}{\sqrt{\xi^2-1}}\psi_m^*\right)\frac{\partial}{\partial\xi}\left(\frac{\xi}{\sqrt{\xi^2-1}}\psi_m\right)+(1-\eta^2)^2\frac{\partial}{\partial\eta}\left(\frac{1}{\sqrt{1-\eta^2}}\psi_m^*\right)\frac{\partial}{\partial\eta}\left(\frac{1}{\sqrt{1-\eta^2}}\psi_m\right)+\left(\frac{m^2-1}{\xi^2-1}+\frac{m^2-1}{1-\eta^2}+2+\frac{2}{\xi^2}\right)\psi_m^*\psi_m\right]-E\int_1^\infty d\xi\int_{-1}^1 d\eta(\xi^2-\eta^2)\psi_m^*\psi_m\right\}=0 \tag{A2}$$

for odd $|m|$. Then we apply pseudospectral discretization to Eqs. (A1) and (A2). The coordinate ξ is mapped to the interval $[-1,1]$ according to the following formulas:

$$\xi=1+R_l\frac{1+x}{1-x+\dfrac{2R_l}{R_b-1}}, \tag{A3}$$

$$\xi'\equiv\frac{d\xi}{dx}=2R_l\frac{1+\dfrac{R_l}{R_b-1}}{\left(1-x+\dfrac{2R_l}{R_b-1}\right)^2}. \tag{A4}$$

Here R_l and R_b are the parameters of the transformation (A3). The parameter R_b is the maximum value of the coordinate ξ; it corresponds to $x=1$. Making this parameter finite, we can solve the problem in the finite volume around the nuclei that significantly improves the accuracy. The zero boundary conditions are imposed on the wave function at $\xi=R_b$. In our calculations we used $R_b=40$. In the time-independent calculations, this value is large enough to ensure high accuracy of sufficient number of both discrete and continuous eigenstates. When solving the time-dependent equation in the laser field, some measures should be taken to prevent an unphysical reflection from the boundary. We use an absorbing layer located between $\xi=20$ and $\xi=40$ which smoothly brings down the wave function and prevents the reflection.

The variable x is discretized using the Legendre-Gauss-Radau scheme (x_j are the collocation points and w_j are the quadrature weights) [18],

$$x_i:\ P_{N_x}(x_i)-P_{N_x+1}(x_i)=0,$$

$$w_i^x=\frac{1}{(N_x+1)^2}\frac{1+x_i}{[P_{N_x}(x_i)]^2}. \tag{A5}$$

Here N_x is the number of collocation points used, $P_{N_x}(x)$ is the Legendre polynomial; the collocation points are obtained as roots of the difference of two polynomials with orders N_x and N_x+1, respectively. The Gauss-Radau scheme allows easily implement boundary conditions at the end of the interval since $x=1$ is always a collocation point, irrespectively of N_x. The integration and differentiation formulas in the Legendre-Gauss-Radau scheme can be written as follows [$f(x)$ is an arbitrary function]:

$$\int_{-1}^1 f(x)dx=\sum_{i=1}^{N_x+1} f(x_i)w_i^x, \tag{A6}$$

$$\frac{df}{dx}(x_i) = \sum_{i'=1}^{N_x+1} D^x_{ii'} f(x_{i'}). \tag{A7}$$

Here the derivative matrix $D^x_{ii'}$ is defined as follows:

$$D^x_{ii'} = d^x_{ii'} \frac{(1+x_{i'})P_{N_x}(x_i)}{(1+x_i)P_{N_x}(x_{i'})}, \tag{A8}$$

$$d^x_{ii'} = \frac{1}{x_i - x_{i'}} \ (i \neq i'), \quad d^x_{ii} = -\frac{1}{2(1+x_i)},$$

$$d^x_{N_x+1,N_x+1} = \tfrac{1}{4}N_x(N_x+2). \tag{A9}$$

The coordinate η does not need any additional mapping transformation since it originally spans the interval $[-1,1]$. However, in the most general case such a transformation can be applied, so we will assume that η is mapped to the variable y within the interval $[-1,1]$ (in practical calculations we used the identity transformation $\eta=y$). Unlike the variable x, we discretize y using the Legendre-Gauss scheme for we do not have to apply any boundary conditions at the points $y = \pm 1$. The collocation points for this scheme are defined as the roots of the Legendre polynomial P_{N_y}, and the quadrature weights are expressed through the derivatives of this polynomial (N_y is the number of collocation points used) [18],

$$y_j\text{: } P_{N_y}(y_j) = 0,$$

$$w^y_j = \frac{1}{(1-y_j^2)[P'_{N_y}(y_j)]^2}. \tag{A10}$$

The integration and differentiation in the Legendre-Gauss scheme are performed as follows [$g(y)$ is an arbitrary function]:

$$\int_{-1}^{1} g(y)dy = \sum_{i=1}^{N_y} g(y_j) w^y_j, \tag{A11}$$

$$g'(y_j) = \sum_{j'=1}^{N_y} D^y_{jj'} g(y_{j'}), \quad D^y_{jj'} = d^y_{jj'} \frac{P'_{N_y}(y_j)}{P'_{N_y}(y_{j'})}, \tag{A12}$$

with the derivative matrix $d^y_{jj'}$ defined as

$$d^y_{jj'} = \frac{1}{y_j - y_{j'}} \ (j \neq j'), \quad d^y_{jj} = \frac{y_j}{1-y_j^2}. \tag{A13}$$

Once the basic expressions of the pseudospectral discretization are established by Eqs. (A5)–(A13), one can proceed to discretize the variational eigenvalue problems (A1) and (A2). The results are given by Eqs. (7)–(11).

[1] P. Salières, A. L'Huillier, P. Antoine, and M. Lewenstein, Adv. At., Mol., Opt. Phys. **41**, 83 (1999).
[2] T. Brabec and F. Krausz, Rev. Mod. Phys. **72**, 545 (2000).
[3] J. H. Posthumus, Rep. Prog. Phys. **67**, 623 (2004).
[4] H. Stapelfeldt and T. Seideman, Rev. Mod. Phys. **75**, 543 (2003).
[5] See, for example, S. I. Chu, J. Chem. Phys. **75**, 2215 (1981); Adv. Chem. Phys. **73**, 739 (1989); L. B. Madsen, M. Plummer, and J. F. McCann, Phys. Rev. A **58**, 456 (1998); X. Chu and S. I. Chu, *ibid.* **63**, 013414 (2000).
[6] See, for example, G. H. Yao, and S. I. Chu, Phys. Rev. A **48**, 485 (1993); T. Zuo and A. D. Bandrauk, *ibid.* **52**, R2511 (1995); A. Giusti-Suzor, F. H. Mies, L. F. DiMauro, E. Charron, and B. Yang, J. Phys. B **28**, 309 (1995); L. Y. Peng, D. Dundas, J. F. McCann, K. T. Taylor, and I. D. Williams, *ibid.* **36**, L295 (2003).
[7] D. A. Telnov and S. I. Chu, Phys. Rev. A **71**, 013408 (2005).
[8] G. Yao and S. I. Chu, Chem. Phys. Lett. **204**, 381 (1993).
[9] X. Chu and S. I. Chu, Phys. Rev. A **63**, 013414 (2000).
[10] X. M. Tong and S. I. Chu, Chem. Phys. **217**, 119 (1997).
[11] A. Staudte, D. Pavičić, S. Chelkowski, D. Zeidler, M. Meckel, H. Niikura, M. Schöffler, S. Schössler, B. Ulrich, P. P. Rajeev, Th. Weber, T. Jahnke, D. M. Villeneuve, A. D. Bandrauk, C. L. Cocke, P. B. Corkum, and R. Dörner, Phys. Rev. Lett. **98**, 073003 (2007).
[12] See, for example, J. Itatani, D. Zeidler, J. Levesque, M. Spanner, D. M. Villeneuve, and P. B. Corkum, Phys. Rev. Lett. **94**, 123902 (2005); D. Pavičić, K. F. Lee, D. M. Rayner, P. B. Corkum, and D. M. Villeneuve, *ibid.* **98**, 243001 (2007); E. Wells, M. J. DeWitt, and R. R. Jones, Phys. Rev. A **66**, 013409 (2002).
[13] X. M. Tong, Z. X. Zhao, and C. D. Lin, Phys. Rev. A **66**, 033402 (2002).
[14] J. Muth-Böhm, A. Becker, and F. H. M. Faisal, Phys. Rev. Lett. **85**, 2280 (2000).
[15] X. Chu and S. I. Chu, Phys. Rev. A **63**, 023411 (2001).
[16] X. Chu and S. I. Chu, Phys. Rev. A **64**, 063404 (2001); **70**, 061402(R) (2004).
[17] J. Heslar, J. J. Carrera, D. A. Telnov, and S. I. Chu, Int. J. Quantum Chem. **107**, 3159 (2007).
[18] *Handbook of Mathematical Functions*, edited by M. Abramowitz and I. Stegun (Dover, New York, 1965).
[19] D. A. Telnov and S. I. Chu, J. Phys. B **37**, 1489 (2004).
[20] L. D. Landau and E. M. Lifshitz, *The Classical Theory of Fields* (Pergamon, Oxford, 1975).
[21] M. M. Madsen and J. M. Peek, At. Data **2**, 171 (1971).
[22] G. L. Kamta and A. D. Bandrauk, Phys. Rev. A **71**, 053407 (2005).
[23] P. B. Corkum, Phys. Rev. Lett. **71**, 1994 (1993); J. L. Krause, K. J. Schafer, and K. C. Kulander, *ibid.* **68**, 3535 (1992).
[24] R. Kopold, W. Becker, and M. Kleber, Phys. Rev. A **58**, 4022 (1998).
[25] M. Lein, N. Hay, R. Velotta, J. P. Marangos, and P. L. Knight, Phys. Rev. A **66**, 023805 (2002).
[26] M. Lein, P. P. Corso, J. P. Marangos, and P. L. Knight, Phys. Rev. A **67**, 023819 (2003).